CAMERA RESPONSE FUNCTION SIGNATURE FOR DIGITAL FORENSICS – PART I: THEORY AND DATA SELECTION

*Tian-Tsong Ng**

Institute for Infocomm Research
Singapore

Mao-Pei Tsui

University of Toledo
Ohio, US

ABSTRACT

Camera response function (CRF) is a form of camera signatures which can be extracted from a single image and provides a natural basis for image forensics. CRF extraction from a single-image is in theory ill-posed. It relies on specific structures in an image that offer glimpses of the CRF. Therefore, the challenges in CRF extraction are first in identifying structures of such property, second in locating such structures in an image, and third in extracting the CRF attributes from the selected structures. In our past work, we proposed that CRF attributes can be found on linear structures in an image and extracted using linear geometric invariants. In this paper, we show additional properties on linear geometric invariants, propose a more robust way to select linear structures in an image, and provide a model-based method to extract CRF attributes from the linear structures. This paper is divided into two parts. Part I is devoted to the theory of linear geometric invariants and the robust selection of linear structures. The linear structure candidates obtained from the method in Part I are used to instantiate the edge profiles for CRF extraction in Part II. The paper as a whole presents a reliable method for CRF extraction, together with rigorous analysis which gives useful insights into the method.

In the first half of Part I, a simpler proof that links the equality of linear geometric invariants to a linear-isophote surface is given. As a by-product, the proof leads to an additional way to detect linear-isophote surfaces which uses only the first-order partial derivatives and improves detection reliability. In the second half of Part I, the variance of linear geometric invariants is shown to have a structure which can be used to improve the robustness in detecting linear-isophote surfaces.

Index Terms— Camera response function, image forensics, geometric invariants, linear-isophote surfaces

1. INTRODUCTION

A major goal of image forensics is to evaluate the authenticity of an image. The *camera signatures* inherent in an image provide a natural basis for image content authenticity. Examples of camera signatures are such as the attributes of the color filter array [1], sensor noise or irregularity [2], and the non-linear response function [3] in a camera. Therefore, image forensics based on camera signatures in general is divided into *two* steps: (1) Extraction of camera signatures from a single image or its segments, (2) Image authenticity assessment based on a set of rules or criteria. The rules could be the consistency of signatures across different segments [3], the irregularities of the signatures on segment boundaries [4], or the disappearance of the typical signatures [1]. To draw a parallel with the distinction between low-level and high-level vision [5], the two steps above can be called *low-level* and *high-level forensics*. Low-level forensics is completely physics-based, while the high-level forensics varies with how users tamper with images (including the post-processing). In this paper, we focus only on low-level forensics for *camera response function* (CRF).

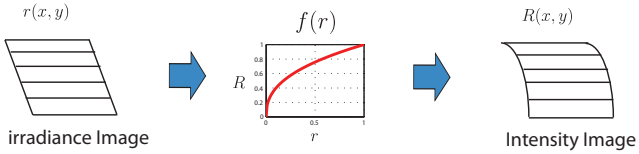

Fig. 1. A curved surface that carries the imprint of the CRF.

A CRF describes how the output of a camera (*image intensity*) responds to the radiant energy incident to and measured by its image sensor (*image irradiance*). A CRF is specific for a model of camera and in general non-linear in order to compress the radiometric dynamic range for keeping the output image visually pleasing. Apart from image forensics, CRF signatures extracted from an image can also be used for CRF estimation. Once the CRF is known, an image can be calibrated such that it becomes radiometrically linear. Such linear image is important for many computer vision methods such as shape from shading, photometric stereo, Helmholtz stereopsis, color constancy, diffuse-specular separation and camera-shake removal [6, 7].

CRF extraction *from a single-image* is challenging and in theory ill-posed. It relies on specific structures in an image that offer glimpses of the CRF. Therefore, the challenges in CRF extraction are in (1) identifying structures that carry

*email: ttng@i2r.a-star.edu.sg. We would like to thank Prof. Shih-Fu Chang for the valuable discussion.

CRF attributes, (2) locating such structures in an image, and (3) extracting the CRF attributes from the selected structures. Structures with CRF attributes being proposed include local image patches with little quadratic phase coupling [8], image edges with linearly blended colors [9], image edges with uniform grayscale histogram [10], linear local surfaces on an image [11], and image regions with symmetric noise distribution [12]. In general, little attention has been given to the localization of these structures. A set of heuristic rules is defined for locating the underlying image edges with linearly blended colors [4] while an equality condition for linear geometric invariants is used for locating locally linear surfaces on an irradiance image [11]. Finally, except for [11], CRF signature is not explicitly extracted as CRF is directly estimated by evaluating its capability in linearizing the data. A host of questions remain unanswered by the prior works. For example: How the underlying structures can be effectively and robustly located in an image? How to show that the CRF methods are general and work consistently on almost all typical natural-scene images?

This paper seeks to address these questions. In Part I, we show an additional way to detect linear-isophote surfaces which uses *only the first-order partial derivatives*, and model the variance of linear geometric invariants for improving the robustness of linear-isophote surface detection. In part II, we show how the selected points on linear-isophote surfaces can be used to instantiate the edge profiles where their interactions effectively point to the desired underlying linear structures. This method requires *no learning from data* and works on both simulation and real camera images.

2. GEOMETRY-INVARIANT FOR CRF SIGNATURE EXTRACTION: FOUNDATION AND ASSUMPTION

In our prior work [11], we identified that local surfaces corresponding to linear surfaces in an irradiance image reveal the local shape of the CRF (see Fig. 1). However, locally linear surfaces are not everywhere in the underlying irradiance image which is unobserved. This leads to a question of how to detect these underlying linear surfaces. Before answering this question, let us introduce a set of *differential quantities* which we called *linear geometric invariants*, $\frac{R_{xx}}{R_x^2}$, $\frac{R_{xy}}{R_x R_y}$, and $\frac{R_{yy}}{R_y^2}$, where $R = R(x, y)$ representing a two dimensional intensity image while R_a and R_{ab} are respectively the first and second-order partial derivatives $\frac{\partial R}{\partial a}$ and $\frac{\partial^2 R}{\partial a \partial b}$.

It was shown that when the underlying irradiance surface is linear, the linear geometric invariants form an equality which is a functional of the CRF, f:

$$\frac{R_{xx}}{R_x^2} = \frac{R_{xy}}{R_x R_y} = \frac{R_{yy}}{R_y^2} = \frac{f''(f^{-1}(R))}{(f'(f^{-1}(R)))^2}. \quad (1)$$

The equality relationship in Eq. 1 gives us a natural equation to detect the underlying linear surfaces. However, it was shown that the equality relationship implies surfaces with linear *isophotes* (i.e., equal intensity contours). Unfortunately, the observation of linear-isophote surfaces is a necessary but not a sufficient indicator from underlying linear surface because any linear-isophote surface (for which a linear surface is a special case) remains a linear-isophote surface after a CRF transformation. As a result, if there exists locally linear surfaces in image irradiance, the equality relationship in Eq. 1 will detect points on these surfaces together with points on the underlying linear-isophote surfaces. Such detection ambiguity is shown in the Venn diagram in Fig. 2.

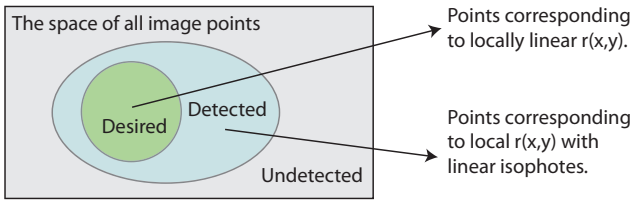

Fig. 2. The equality relationship of linear geometric invariants detects the set of points on linear-isophote surface.

The proof that links the equality relationship in Eq. 1 to linear-isophote surfaces given in [11] was complicated. We give a simpler proof for the relationship as stated in Proposition 2 which uses Proposition 1.

Proposition 1. *In the neighborhood about a point p, the relationship $\frac{R_{xx}}{R_x^2} = \frac{R_{xy}}{R_x R_y} = \frac{R_{yy}}{R_y^2}$ for a surface $R(x, y)$ implies that the orientation of the gradient vectors in the neighborhood is uniform, up to a sign.*

Proof. We assume that $R_x \neq 0$ and $R_y \neq 0$ in a neighborhood about the point p. If the relationship $\frac{R_{xx}}{R_x^2} = \frac{R_{xy}}{R_x R_y} = \frac{R_{yy}}{R_y^2}$ holds in the neighborhood, then so do the relationships $R_{xx}R_y = R_{xy}R_x$ and $R_{yy}R_x = R_{xy}R_y$. This implies that the partial derivatives of $\frac{R_x}{R_y}$ are zero in the neighborhood as shown below:

$$\frac{\partial}{\partial x}\left(\frac{R_x}{R_y}\right) = \frac{R_{xx}R_y - R_{xy}R_x}{R_y^2} = 0 \quad (2)$$

$$\frac{\partial}{\partial y}\left(\frac{R_x}{R_y}\right) = \frac{R_{xy}R_y - R_{yy}R_x}{R_y^2} = 0 \quad (3)$$

This implies that $\frac{R_x}{R_y}$ = constant and the gradient direction (not magnitude) in the neighborhood of $R(x, y)$ is constant up to a sign. □

Proposition 2. *If the relationship $\frac{R_{xx}}{R_x^2} = \frac{R_{xy}}{R_x R_y} = \frac{R_{yy}}{R_y^2}$ holds for a surface $R(x, y)$ in a neighborhood about a point p, then $R(x, y)$ is a local surface with linear isophotes (i.e., equal intensity contours) at p.*

In addition, there exists an invertible and differentiable function $h : \mathbb{R} \mapsto \mathbb{R}$, such that $h^{-1}(R(x, y))$ is a locally linear surface in the neighborhood of p, and we can write

$$\frac{R_{xx}}{R_x^2} = \frac{R_{xy}}{R_x R_y} = \frac{R_{yy}}{R_y^2} = \frac{h''(h^{-1}(R))}{(h'(h^{-1}(R)))^2} \text{ at } p. \quad (4)$$

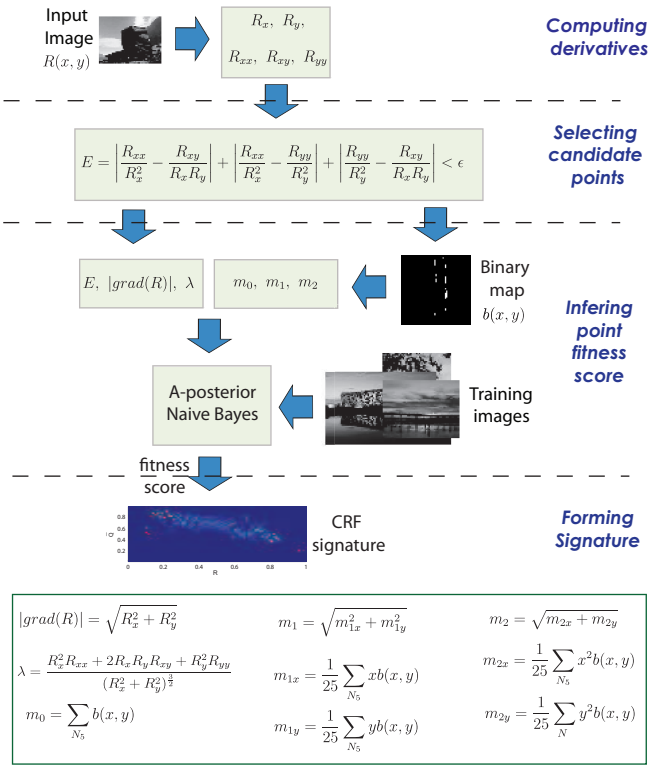

Fig. 3. The computational steps for the method in [11].

Proof. From Proposition 1, we know that if the relationship $\frac{R_{xx}}{R_x^2} = \frac{R_{xy}}{R_x R_y} = \frac{R_{yy}}{R_y^2}$ holds for a surface $R(x,y)$ in a neighborhood about p, then we have $\frac{R_x}{R_y} = \mathrm{c}$ and $R_x = \mathrm{c}R_y$ in the neighborhood, where c is a constant.

The constant coefficient 1st-order partial differential equation (PDE) of the form $R_x = \mathrm{c}R_y$ or $-R_x + \mathrm{c}R_y = 0$ has a solution $R(x,y) = h(\mathrm{c}x + y)$ [13] for some differentiable and invertible function $h : \mathbb{R} \mapsto \mathbb{R}$.

Since $\mathrm{c}x + y$ is linear and the function h preserves the linear isophote of $\mathrm{c}x + y$, then $R(x,y)$ is a local surface with linear isophotes at the neighborhood of p. Furthermore, we can write Eq. 4. □

3. CANDIDATE POINT SELECTION

Fig. 3 shows how a CRF signature was obtained in [11]. Given a grayscale input image $R(x,y)$, the derivatives were computed by fitting the image function with a smoothing cubic spline. Then, an initial set of candidate points was selected using the error function E which measures how well the equality in Eq. 1 is satisfied and produces a binary location map of the selected points. As shown Fig. 2, the selected points include the unwanted points on non-linear surfaces with linear isophotes in image irradiance. In [11], Naive bayes inference was performed to weigh down the unwanted points with a fitness score. The inference was based on six features, as shown in Fig. 3, which include local spatial moments m_{0-2} from the binary map $b(x,y)$, error function value E, gradient magnitude $|grad(R)|$, and the normalized second-order derivative in the gradient direction λ. The prior distribution of the features was obtained from a set of training images. Finally, the CRF signature was given by the histogram of the fitness scores in R-$\bar{Q}$ space where $\bar{Q}$ is defined below:

$$\bar{Q}(R) = \frac{\sqrt{3}}{\sqrt{3}-1}\left(1 - \sqrt{\frac{1}{2Q(R)+1}}\right), \tag{5}$$

$$\text{where} \quad Q(R) = \frac{1}{1 - \frac{1}{3}\left(\frac{R_{xx}}{R_x^2} + \frac{R_{xy}}{R_x R_y} + \frac{R_{yy}}{R_y^2}\right)R}. \tag{6}$$

$\bar{Q}$ is obtained by linearizing $Q(R)$ with respect to the differential change of the gamma curve parameter, γ.

The error function E shown in Fig. 3 depends significantly on the accuracy of the second-order derivative estimation and has not taken the variance of the invariant difference into account. In Sec. 3.1 and 3.2 of this Part I, we address the above-mentioned issues. The issue of distilling the underlying linear surfaces from the candidate set and forming CRF signature will be addressed in Part II of this paper.

3.1. Candidate Point Selection using First-order Derivatives

The error function E shown in Fig. 3 depends significantly on the accuracy in estimating the second-order derivatives of $R(x,y)$. Estimation of second-order derivatives is definitely noisier than that of first-order derivatives. Proposition 1 suggests a solution to the problem: the equality relationship can be equivalently evaluated by examining how well the gradient field in a neighborhood is aligned. Note that only the first-order derivatives are needed. The alignment of a local gradient field about a point p can be measured as below:

$$S_1 = 1 - \left| \sum_{(x,y)\in\mathcal{N}_p} w_p(x,y) \frac{grad(R)}{|grad(R)|} \right| \tag{7}$$

where $w_p(x,y)$ is a gaussian function center at p and $S_1 = 0$ when the gradients are fully aligned. Eq. 7 also imposes a monotonicity condition (the sign counts) which is a stronger statement than that of Proposition 1. The constraint is reasonable as most of the CRF's are monotonic and its action on a linear surface results in a monotonic surface.

Having S_1, candidate point selection would become less sensitive to the accuracy of the second-order derivatives. As a result, we can use a *fast* derivative estimator [14] without worrying too much about its higher-order accuracy.

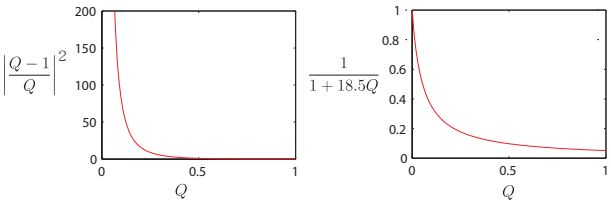

Fig. 4. The similar shape for $(\frac{Q-1}{Q})^2$ and $\frac{1}{1+18.5Q}$

3.2. Considering Error Function Variance

If the geometric invariants are multiplied by a scalar factor, the error function E in Fig. 3 will be scaled by the same factor. Ideally, the scaling factor is immaterial as E on a local surface with linear isophotes is always zero. However, due to computational errors and imperfect local surfaces, E would be small but non-zero in this case. Hence, the scaling factor has an effect.

From Eq. 1, the value of the invariants depends on the CRF f which is a function of R. To model such variance, we study the scaling effect using gamma curves $R = r^\gamma$. In a neighborhood of linear $r(x, y)$, the invariants are as below:

$$\frac{R_{xx}}{R_x^2} = \frac{R_{xy}}{R_x R_y} = \frac{R_{yy}}{R_y^2} = \frac{\gamma - 1}{\gamma R} = \frac{Q-1}{QR}, \tag{8}$$

where in the special case of gamma curves, we have $\gamma = Q(R)$ (see Eq. 6). Eq. 8 indicates that the scale of the invariants depends on both $Q(R)$ and R, and we can infer that the invariant difference would have a similar scaling property. Hence, we can redefine the error function in the form of Mahalanobis distance [15] which takes the invariant variance into account:

$$S_2 = \sqrt{d^t C^{-1} d}, \tag{9}$$

where $d = (\frac{R_{yy}}{R_y^2} - \frac{R_{xy}}{R_x R_y}, \frac{R_{xx}}{R_x^2} - \frac{R_{yy}}{R_y^2}, \frac{R_{xy}}{R_x R_y} - \frac{R_{xx}}{R_x^2})$ and $C = \frac{1}{1+18.5Q}\frac{1}{R^2} I$, with I being the identity matrix. In Eq. 9, we approximate the variance with $\frac{1}{1+18.5Q}\frac{1}{R^2}$ where $\frac{1}{1+18.5Q}$ has a similar shape as $(\frac{Q-1}{Q})^2$ (see Eq. 8), as shown in Fig. 4. Only the general trend of the function needs to be modeled.

With S_1 in Eq. 7 and S_2 in Eq. 9, we select candidate points as below:

$$w_g = G(S_1; \sigma_{S_1}) G(S_2; \sigma_{S_2}) > w_{thres} \tag{10}$$

where $G(\cdot; \sigma) = \frac{1}{\sqrt{2\pi\sigma^2}} \exp\left(-\frac{(\cdot)^2}{2\sigma^2}\right)$ is a zero-mean gaussian function, and the maximum possible value for w_g is $w_{gmax} = G(0; \sigma_{S_1}) G(0; \sigma_{S_2})$.

4. EXPERIMENTS ON GAMMA IMAGES

In this Section, we seek to verify our method through simulation using linear images transformed by gamma curves $R = f(r) = r^\gamma$. Using gamma images makes evaluation easy as their ground-truth CRF is definite. The linear images are of natural scenes, captured using a Canon G3 camera in RAW format from which the uncompressed TIFF format images are extracted using the Canon software. We have verified using a Macbeth color checker that images obtained this way are radiometrically linear.

With a more robust candidate point selection method, we can afford to use a faster local polynomial derivative estimator [14] which unlike B-spline derivative estimator it does not ensure spatial continuity in the estimated derivatives. In Matlab, the former takes only 5 seconds to compute the first and second-order derivatives on one image, while the latter takes 240 seconds.

Fig. 5 shows the candidate point distributions from two images in R-$\bar{Q}$ space. The top image has more straight edges of various intensity compared to the bottom one. This explains why the distributions for the top image span a larger extent in R axis as compared to those for the bottom image. Fig. 5 shows that without considering the variance of invariant difference in candidate point selection a lot of high R-value points are selected. From Eq. 8, the invariant magnitude scales with $1/R$, hence with a fixed selection threshold, more high R-value points are selected as these points tend to have a lower variance. It can be seen that after considering the variance in point selection, less high R-value points are selected and the distributions become more balanced.

It is likely that the difference of invariants at a point is small in magnitude but the local gradients are not aligned. It can be due to inaccurate second-order derivative estimation and the invariants at some of the non-linear isophote surfaces have unusually low value. These points are picked up by the gradient uniformity measure in Eq. 7 and shown to be outliers in Fig. 6.

It is also observed in Fig. 5 that the distributions are slanted to the left, and after accounting for the variance the distributions are shifted upward slightly and becomes more centered on the ground-truth line for the gamma curves. Having a selection function in Eq. 10 alone, despite the $1/R$ scaling compensation, cannot explain for the upward shifting. We will show in Part II of this paper that the candidate points do not just scatter randomly in the spatial domain of an image. In fact, the candidate points gather in the neighborhood of straight edges and can be grouped into edge profiles where the gradient of the points in an edge profile is aligned. The R-$\bar{Q}$ profiles derived from the edge profile are of a shape slanted to the left. This explains why the distributions are slanted to the left. Having this structure, compensating for the $1/R$ scaling in Eq. 10, the R-$\bar{Q}$ profiles would appear to shift upward. More details about the edge profile structure are given in Part II of this paper.

5. COMMENTS ON PART I

We began by presenting the idea of extracting the CRF signature from surfaces linear in image irradiance using linear geometric invariants. We gave a simpler proof showing that linear geometric invariants only enable us to detect linear-isophote surfaces. From the proof we show that the equality relationship of the invariants can be equivalently evaluated us-

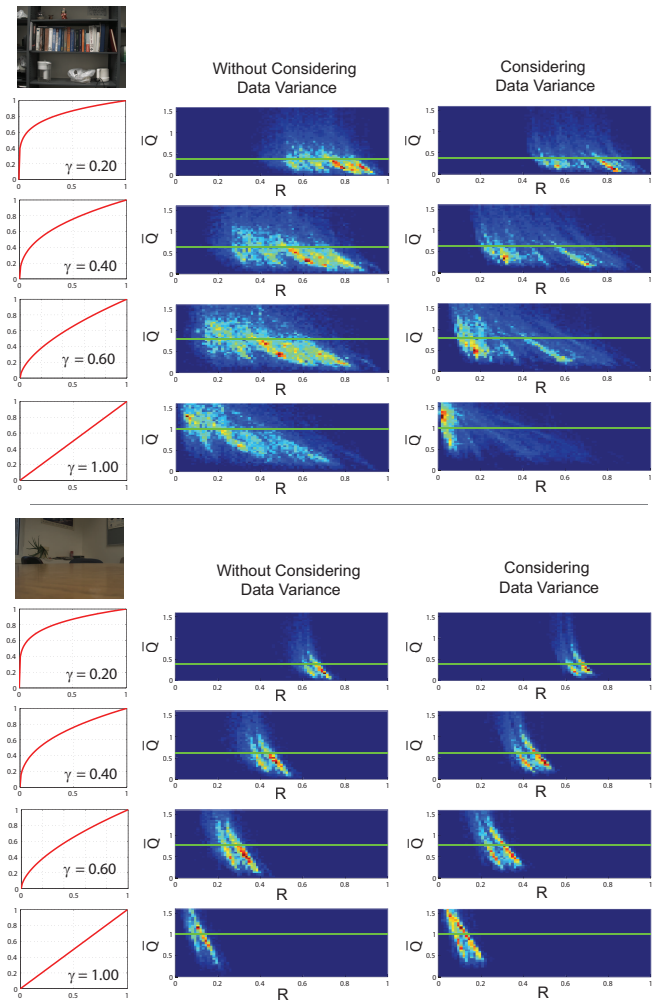

Fig. 5. Distributions of candidate points selected without considering the variance of invariant difference (left column) and after considering the variance (right column). The horizontal lines are the ground-truth R-$\bar{Q}$ lines corresponding to the gamma curves.

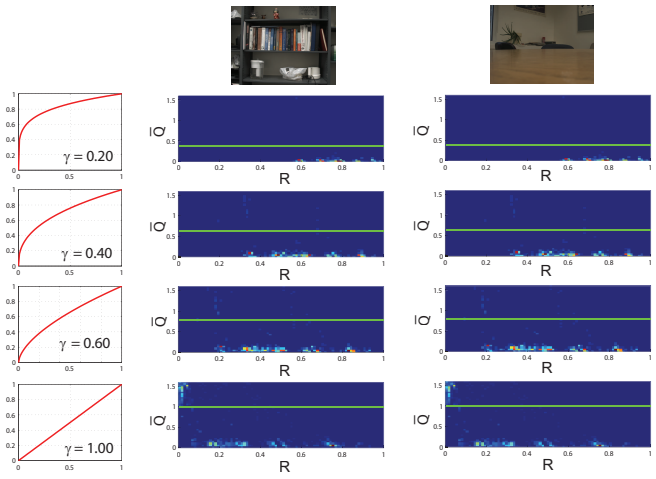

Fig. 6. Right column shows points that pass the invariant equality threshold but not the gradient uniformity threshold. The horizontal lines are the ground-truth R-$\bar{Q}$ curves corresponding to the respective gamma curves.

ing only first-order derivatives. This reduces our dependency on second-order derivatives for selecting points on linear-isophote surfaces and enables the use of fast local-derivative estimators.

We also showed that evaluating the equality relationship of the invariants without considering their variance would make the candidate point selection biased towards points with small variance. In experiments, we showed that by incorporating the variance into point selection help producing a point distribution which is more balanced and well-centered on the ground-truth curves.

To understand the consistently left-slanted distributions in R-$\bar{Q}$ space, we need to introduce the edge profile structure within the candidate point set in Part II. We will show how the edge profile structure could help in identifying the points on the underlying linear surface, given the candidate point set.

6. REFERENCES

[1] A. C. Popescu and H. Farid, "Exposing digital forgeries in color filter array interpolated images," *IEEE Transactions on Signal Processing*, vol. 53, no. 10, pp. 3948–3959, 2005.

[2] J. Lukas, J. Fridrich, and M. Goljan, "Detecting digital image forgeries using sensor pattern noise," in *SPIE Electronic Imaging, Photonics West*, January 2006.

[3] Y.-F. Hsu and S.-F. Chang, "Detecting image splicing using geometry invariants and camera characteristics consistency," in *IEEE Intl Conf. on Multimedia and Expo*, 2006.

[4] Z. Lin, R. Wang, X. Tang, and H.-Y. Shum, "Detecting doctored images using camera response normality and consistency," in *IEEE CVPR*, 2005.

[5] D. A. Forsyth and J. Ponce, *Computer Vision: A modern approach*, Prentice Hall Professional Technical Reference, 2002.

[6] R. Fergus, B. Singh, A. Hertzmann, S. T. Roweis, and W. T. Freeman, "Removing camera shake from a single photograph," in *ACM SIGGRAPH*, 2006.

[7] B. K. P. Horn, *Robot vision*, MIT Press, Cambridge, MA, USA, 1986.

[8] H. Farid, "Blind inverse gamma correction," *IEEE Trans. Image Processing*, vol. 10, no. 10, pp. 1428–1433, 2001.

[9] S. Lin, J. Gu, S. Yamazaki, and H.-Y. Shum, "Radiometric calibration from a single image," in *IEEE CVPR*, 2004.

[10] S. Lin and L. Zhang, "Determining the radiometric response function from a single grayscale image," in *IEEE CVPR*, 2005.

[11] T.-T. Ng, S.-F. Chang, and M.-P. Tsui, "Using geometry invariants for camera response function estimation," in *IEEE CVPR*, 2007.

[12] Y. Matsushita and S. Lin, "Radiometric Calibration from Noise Distributions," in *IEEE CVPR*, 2007.

[13] W. A. Strauss, *Partial Differential Equations: an Introduction*, Wiley, 1992.

[14] T. Vieville and O. D. Faugeras, "Robust and fast computation of unbiased intensity derivatives in images," in *ECCV*, 1992.

[15] R. O. Duda, P. E. Hart, and D. G. Stork, *Pattern Classification*, Wiley-Interscience Publication, 2000.